Single-cell profiling of EZH2-mediated immune signaling perturbations in NSCLC

Daniel R. Plaugher[1,#], Avery R. Childress[1], Christian M. Gosser[1], Dave-Preston Esoe[1], Jinpeng Liu[2], Christine F. Brainson[1,3,#]

[1] Department of Toxicology and Cancer Biology, University of Kentucky, Lexington KY 40536 USA

[2] Department of Cancer Biostatistics, University of Kentucky, Lexington, Kentucky.

[3] Markey Cancer Center, University of Kentucky, Lexington KY 40536 USA

[#] Corresponding authors:

Daniel R. Plaugher - plaugher_dr@uky.edu

Christine F. Brainson - cfbrainson@uky.edu

averychill20@uky.edu, christiangosser@uky.edu, davepreston.esoe@uky.edu, jinpeng.liu@uky.edu

Keywords: non-small cell lung cancer, cell signaling, immune micro-environment, epigenetics, tumor-infiltrating lymphocytes

Abstract

Lung cancer remains a significant public health burden. One of the most personalized treatments uses a patient's own tumor infiltrating lymphocytes (TILs), and TIL activity is also essential for immune checkpoint inhibitor (ICI) effectiveness. Responses to immunotherapies vary due to immune-suppressive tumor microenvironments (TMEs) and limited antigen presentation. In this study, we computationally examine cell-cell signaling and transcriptional activity using single-cell RNA sequencing of lung cancer treated by inhibiting methyltransferase EZH2. We show that EZH2 inhibition shifts the TME to immunogenic signaling patterns conducive to increased T cell response, including antigen presentation and homing. T cells also showed more stem-like phenotypes. Transcriptional activity was quieter with EZH2 inhibition but revealed better interferon response, altered myeloid and B cell differentiation, and apoptotic markers. Importantly, inferred EZH2 activity showed it could perform non-methyltransferase duties vital for T cell differentiation. These results indicate that EZH2 inhibition could improve immunotherapies for lung cancer patients.

Main

Lung cancer remains the leading cause of cancer-related death in the U.S. among both men and women. With a combined 131,889 deaths in 2022, lung cancer's closest competitor for total deaths is in colon/rectum at 52,967 deaths[1]. While survival rates have slowly climbed due to advances in therapy and early detection, they remain at a 5-year relative rate of 27%. Lung cancer is well known for its immense heterogeneity, leading to limited effective treatment options. However, there is a silver lining; NSCLC is highly mutated, and thus is a vulnerable due to the high rate of neo-antigen presentation for T cell recognition[2, 3].

Novel immunotherapeutic techniques including anti-PD/PD-L1 immune checkpoint inhibitor (ICIs) and adoptive cell transfer (ACT) have emerged as effective therapies for many cancer types. While anti-PD1/PD-L1 antibodies rely on endogenous T cell activities, ACT is a "living" treatment, where lymphocytes are infused into a patient and continue to expand after administration (more than 1000-fold)[2]. Chimeric antigen receptor T cell (CAR-T) and modified T cell receptor (TCR) therapies are designed to recognize a specific (neo)antigen, an approach that has fallen short in solid tumors due to lack of common antigens among patients[4]. Tumor-infiltrating lymphocyte (TIL) therapy is polyclonal by nature, and is arguably the most personalized form of cancer therapy. With respect to NSCLC, it is currently unknown what tumor genotypes and phenotypes will respond best to TIL therapy, but numerous trials combining ICIs and TIL therapy are underway – including studies investigating epigenetic modulation.

A key challenge for both TIL and ICI therapies is to maintain T cell stemness and resist exhaustion, while also ensuring the patient's tumor microenvironment (TME) is immunogenic. These phenotypes can be controlled through epigenetic mechanisms. For example, DNA and histone methylation are typically associated with gene silencing[5]. Indeed, multiple studies over decades of research have shown the importance of EZH2 (enhancer of zeste homolog 2) in its role as the catalytic subunit of the Polycomb Repressive Complex 2 (PRC2), where it tri-methylates histone 3 at lysine 27 (H3K27me3) through its SET domain. Therapeutic options targeting EZH2

inhibition (EZH2i) include, but are not limited to, GSK126[6], tazemetostat[7, 8], and valemetostat[9] (a dual EZH1/2 inhibitor. An incredibly important point to note is that these inhibitors do not act as knock-out drugs, but rather are specifically geared to target the SET domain and still allow non-methyltransferase activities. This distinction is key because studies have shown that *deletion* of *Ezh2* can restrict memory T cell function and drive terminal differentiation [10, 11]. However, other studies have shown that EZH2 *deletion* can reprogram regulatory T cells (T_R) to T-effector cells (T_{EFF}), and lead to de-repression of transcription factors *Tcf7* and *Id3* important for memory T cells (T_M) [10, 12-14]. Regardless, it is clear that EZH2 within PRC2 is an actionable therapeutic target, and maintaining EZH2 activity outside the complex is also important.

Recently, multiple groups have shown that EZH2i enhances CAR-T and ICI therapies. Specifically, Hou et. al.[15] demonstrated that transient EZH2i promotes progenitor-like T cells without compromising cell expansion. They further revealed that EZH2i improves *in vivo* proliferation, homeostasis, and recall response of ACT T cells, while also showing that there were less-differentiated T cells in human PBMCs and that CAR T-cell exhaustion was alleviated. Then subsequently Porazzi et al. [16] showed similar results such that EZH2 and EZH1/EZH2 inhibition improves the anti-tumor efficacy of CAR-T- and TCR T cell-based therapies against multiple liquid and solid tumors. In our own study[17], we exhibited that EZH2i can increase immune checkpoint inhibitor (ICI, specifically anti-PD1) response in lung squamous cell carcinomas (LSCCs) using tazemetostat and GSK126 as a tool compound. Our *in vitro* experiments using 2D human cancer cell lines, and 3D murine and patient-derived organoids all showed that EZH2i leads to up-regulation of both major histocompatibility complex class I and II (MHCI/II) expression at mRNA and protein levels. We then used ChIP-sequencing to confirm the loss of EZH2-mediated histone marks, as well as the gain of activating histone marks at key loci. Within murine autochthonous (**FIGURE-1A**) and syngeneic LSCC models, we demonstrated robust tumor control with ICI+EZH2i combination therapy.

Of importance to this paper, we performed single-cell RNA-sequencing (scRNAseq) of both lung tumors and total lung. As a brief summary of the study design and initial results[17], fresh autochthonous lung tumors (malignant) were analyzed after four weeks of treatment (Veh-M , EZH2i-M, anti-PD1-M, Combo-M), with premalignant total lung (PM) groups as additional controls (Veh-PM, EZH2i-PM). When comparing Veh-M to Combo, we saw significant decreases in tumor cells, and in some macrophage and neutrophil populations (**FIGURE-1B**). In contrast, we saw significant increases in T cells, cycling cells, normal lung, and some anti-tumor neutrophil populations. From the tumors and total lungs, we identified 16 unique cell populations that were annotated based on conserved markers.

Despite these advances, our prior study largely focused on myeloid compartments and lacked a mechanistic, systems-level view of how the immune TME changes under EZH2 inhibition. Here we use a top-down approach—beginning broadly with cell-cell signaling, narrowing to pathways, and then resolving to cell-type-specific pathways and transcription factor (TF) activity—to understand how EZH2 inhibition remodels the TME

to support T cell responses. These insights are critical to determine whether EZH2 inhibition can effectively augment T cell-based immunotherapies for lung cancer patients.

For this current study we focus only on cohorts of vehicle (Veh-PM/M) and GSK126-treated (EZH2i-PM/M) (**FIGURE-1C**). We first present inferred cell-cell communication alterations using CellChat[18] and LIANA[19], with a primary focus on endogenous TILs (eTILs) that have not undergone *ex vivo* manipulation and infusion as in TIL therapy. These eTILs were originally classified as 'T cells' and 'T cells 2', but for clarity we will refer to them as 'Tcells1' and 'Tcells2' throughout this manuscript. Furthermore, we investigate changes in TF activity using tools like SCENIC[20], BITFAM[21], and CollecTRI[22]. Given that samples for Veh-PM and EZH2-PM were pre-malignant while Veh-M and EZH2-M were malignant, we will focus on pairwise changes among conditions.

Cell-cell signaling patterns shift after EZH2 inhibition

To gain a broad view of cellular communications, we employed CellChat[18] to infer interactions (and strength of interaction) among ligands-receptor pairs and their cofactors with LIANA[19] as a complementary method. We first see that groups Veh-PM, EZH2-PM, and Veh-M have approximately the same number of interactions, but EZH2i-M interactions drop by nearly one-third. However, strengths of interactions drop dramatically in both EZH2i groups (**FIGURE-2A**). In **FIGURE-2B** we show direct cell-cell communications among the 16 unique cell types, with a focus on Tcells1 and Tcells2 to avoid visual clutter. Here, edge colors are consistent with senders, edge weights are proportional to interaction strength, and circle sizes are proportional to the number of cells in each cell group. A deeper dive using differential heatmaps reveals explicitly which cell-cell signals are changing, where red (or blue) represents increased (or decreased) signaling in treatment compared to vehicle (**FIGURE-2C**). The top-colored bar plot represents the column sum of values displayed in the heatmap (incoming signaling) and right colored bar plots represent the sum of row of values (outgoing signaling).

When comparing EZH2i-PM versus Veh-PM, we generally see a decrease in most neutrophil population signaling, but increases in macrophage (1/2), dendritic, proliferating, and Neu-5. Importantly, we previously showed that Neu-1, Neu-4, and Neu-5 express genes such as *Tnf*, *Cxcl10*, and numerous IFN-response genes[17]. Tcells1 only has increased signaling with Neu-5 and decreases elsewhere, but Tcells2 has increased communication with anti-tumor neutrophils, proliferating cells, autocrine signaling, Macs 1, and dendritic cells. Therefore, TME signaling is shifted to be more immunogenic. In contrast, differential signaling of Veh-M versus EZH2i-M nearly all decreases with the interesting exception of eTILs and dendritic cells. We see very distinct increases in outgoing signals of Tcells1, Tcells2, and dendritic cells, and perhaps most importantly there is increased tumor signaling unique to only eTILs (CEACAM, MHC-I, CXCL, KLK, and ADGRE pathways). Changes to malignant cell-type signaling patterns are shown in **SUPPLEMENTARY FIGURES-1&2.**

EZH2 inhibition induces dynamic pathway communication

Next, we identified conserved and context-specific signaling pathways among all cell types by comparing information flow, determined by the sum of communication probabilities among all pairs of cell groups (the total weights in the network). We can identify signaling pathways that turn off, decrease, turn on, or increase by

changes to their information flow when comparing conditions (**FIGURE-3A**). Highly significant signaling pathways ($p<0.01$) were ranked based on differences in the overall information flow within the inferred networks between treatment groups. The top signaling pathways colored gray are enriched in Veh-M, blue is enriched in EZH2i-M, and text colored black indicates an enriched pathway in both groups. First, it is apparent that EZH2i results in fewer enriched pathways (14) compared to Veh-M (43). There is a loss of 14 pathway signals (e.g. CD52, COLLAGEN, ADGRG, NOTCH, LAMININ…etc.) and 7 gained (FASLG, DHT, KLK, Testosterone, CD6, 12oxoLTB4, PD-L1) when treatment is applied. We also see a loss (or decrease) of many pathogenic pathways after treatment such as collagen and fibronectin that play major roles in pulmonary fibrosis, and an increase in immune infiltration pathways like CEACAM, MHC-I, LCK, and THY1.

Network centrality scores of pathways allow us to visualize the roles of pathway signals, for example, MHC-I (**FIGURE-3B**). Here we see a dramatic increase in its role as an influencer (outgoing), as well as a receiver and mediator for eTILs. Likewise, we can investigate pathway cell-cell signal changes after treatment. The CEACAM pathway has been shown to positively correlate with immune infiltration[23], and in **FIGURE-3C** we see that immune signaling increases primarily to eTILs from the tumor and lung epithelium. On the other hand, fibronectin signals of FN1 are decreased and much quieter after treatment (**FIGURE-3D)**.

EZH2 inhibition alters transcription factor activity

The SCENIC[20] pipeline was used to infer transcriptional modifier activity between treatment groups, with BITFAM[21] and CollecTRI[22] as secondary approaches (**SUPPLEMENTARY**). Note that some "TFs" in the SCENIC database are more accurately identified as modifiers (e.g. *Dnmt1, H2faz, …etc.)* but will still be referred to as TFs for ease. Each group has distinct activity, shown with a max-normalized distribution (**FIGURE-4A**). First, EZH2 inhibition does not appear to dramatically shift the number of active translational programs, but rather the factors that make up their regulons. Veh-PM has 46 regulons, an average target magnitude of 130.3 (largest is *Tfec* with 514 targets), and is led by *Mef2c*, *Ebf1*, and *Pax5* – favoring B cell development. Veh-M has 43 regulons, an average target magnitude of 142.1 (largest is *Irf8* with 656 targets), and is led by *Egr1*, *Foxb*, and *Atf3* – indicating stress response and differentiation. EZH2i-PM has 49 regulons, an average target magnitude of 122.9 (largest is *Irf8* with 603 targets), and is led by *Ddit3*, *Jdp2*, and *Atf3* – favoring stress response and apoptosis. Lastly, EZH2i-M has 47 regulons, an average target magnitude of 123.4 (largest is *Irf8* with 625 targets), and is led by *Elf5*, *Yod1*, and *Irf7* – indicating interferon response and inflammation.

Relative to each treatment arm, we see that EZH2i has less enriched TF activity compared to vehicle (**FIGURE-4B**). Examination of greatest changes in log2FC shows that EZH2-PM versus Veh-PM has decreases in *Pbx1* (-5.4), *Ebf1* (-4.9), and *Pax5* (-4.5), with increases in *Jdp2* (1.5), *Nr1h3* (1.4), and *Ddit3* (1.4). That is, we see a decrease in B cell differentiation factors and an increase in stress response, lipid metabolism, and apoptosis. EZH2-M versus Veh-M has decreases in *Fosb* (-5.8), *Nfia* (-2.7), and *Ebf1* (-2.1), with increases in *Cebpa* (4.4), *Maf* (1.9), and *Atf5* (1.6). These show a decrease in developmental factors with a shift in myeloid differentiation and stress response.

Complementary analysis (**SUPPLEMENTARY**) includes Regulon Specificity Score (RSS) that calculates cell type-specific regulon activity, regulon size and target comparisons, and regulon correlation. For example, RSSs of eTILs are shown in **SUPPLEMENTARY FIGURE-3**. Together this provides regulon statistics and cell type composition.

Gene regulatory networks become more granular with EZH2 inhibition

As part of the pySCENIC pipeline, GRNboost2 generates directed and weighted TF-target estimates that we used to build a gene regulatory network (GRN). We have taken these signals and converted them into interactive GRNs of the top 500 communications (see GitHub), as well as performed network analysis for connectivity, connected components (weak and strong), structure, centrality, and motifs. Comparing cohorts with malignant TMEs, we see shifts in network features. First, EZH2i appears to make the GRN more fragmented, as the 500 interactions are spread between 477 unique genes (53 TF only, 398 target only, 26 dual-role) compared to 440 in Veh-M (49 TF only, 367 target only, 23 dual-role). These interactions contain 38 components (largest 269, 7 multi-node strong) and 30 (largest 303, 5 multi-node strong) for treatment and vehicle, respectively. Importance scores have means of 7.9 for vehicle and 7.3 for treatment (*p=0.07*, Cliff's $\delta = 0.067$). Regulators with the highest out-degree between both cohorts remain similar, however, slight decreases in *Irf7* and *Arg1* are observed while having increases in *Irf8*, *Zeb2*, and *Bhlhe41*. This may indicate a decrease in immune suppression through polarization of myeloid populations and enhanced immune signaling. Further, EZH2 inhibition leads to the emergence of mutual regulation of *Lef1* and *Tcf7* – possibly indicating the reprogramming of immune cells into a more stem-like phenotype.

A useful feature of dynamical systems analysis is that elements of the GRN can be targeted to drive the system to a preferred state using *phenotype control theory* [24]. Given that our GRNs are data-driven, they do not inherently contain functional equations (i.e. update rules) to use methods like computational algebra [25] or stable motifs [26]. However, strongly connected components (SCC) allow us to infer potential targets with a feedback vertex set using strictly the topology of a network[27]. Given the SCC of the Veh-M network (diseased state), targets such as *Arg1* (immune suppression) or *Hspa5* (tumor survival) arise as potential therapeutic vulnerabilities of the overall system. Arginase 1 (ARG1) suppresses immune response by catabolizing arginine, which is essential for T cell activation and proliferation[28]. HSPA5 (heat shock 70kDa protein 5) is an endoplasmic reticulum (ER) chaperone that is highly expressed under ER stress and protects cancer cells from ferroptosis and apoptosis[28]. Importantly, while these elements still exist in the treatment GRN, they are much less prevalent and influential.

Ezh2 transcription factor activity is maintained despite methyltransferase inhibition

To determine if SET domain inhibitors also shut down TF activity, we focused specifically on inferred *Ezh2* TF activity with SCENIC. Note that expression level does not imply activity level[20]. Overall, *Ezh2* had 114 inferred targets in Veh-PM, 147 in EZH2-PM, 202 in Veh-M, and 112 in EZH2i-M. We show how these targets overlap

with a 4-way Venn diagram (**FIGURE-5A**). Interestingly, the treatment groups share 7 unique inferred TF activities that include *Calu*, *Cks2*, *Far1*, *Hist1h3d*, *Il11ra1*, *Nav2*, and *Slc7a2*.

Overall activity varies slightly between inference techniques (**FIGURE-5B**), but in general we see little fluctuation within pairwise comparisons. However, it is evident that the malignant environment impacts the TF activity of *Ezh2*. Between cell types (**FIGURE-5C**), proliferating cells see the most *Ezh2* activity across all treatment types. This is expected as EZH2 is involved in cell cycling processes. Specific to eTILs, treatment groups see the most *Ezh2* activity in Tcells1 but Tcells2 are more variable. Similarly, BITFAM and CollecTRI both show that eTILs increase *Ezh2* activity (even though systemic activity is down) in treatment groups when compared to vehicle (**SUPPLEMENTARY**).

Lastly, to show the complex nature of EZH2 communications, we again implemented GRNboost2 to generate interaction networks focused around the top 100 *Ezh2* interactions where edges are weighted by importance scores (**FIGURE-5D**). Here we indicate target genes (green), transcription factors signaling to *Ezh2* (blue), and dual-role actors (crosstalk with *Ezh2* – purple). An interactive version is available (see GitHub). Within the Veh-M group, there is one dual action from *Dtl*, and two other TFs (*Nfix* and *Ehf*). The most important interactions are from *Ezh2* to *Nrarp*, *Sparcl1*, *Serping1*, *Eln*, and *Col14a1*. On the other hand, EZH2i-M has two dual actors (*Foxq1* and *Sox4*) and also had 8 other TFs (*Nap1l1*, *Tagln2*, *Foxm1*, *Dnmt1*, *Dtl*, *H2afz*, *Ehf*, *Egr2*). The most important interactions are from *Ezh2* to *Ttk*, *Brip1*, *Aspm*, and *Chst1*, as well as from *Sox4* to *Ezh2*. Notably, Veh-M has an average importance score of 3.04 but EZH2i-M has an average of 1.94 across the top 100 interactions ($p = 4.66 \times 10^{-11}$, Cliff's $\delta = 0.54$).

Endogenous TIL signaling landscape is reprogrammed after EZH2 inhibition

As a continued point of distinction, when referring to TILs in this context, we are referencing the endogenous infiltrates (eTILs) which we have subset from our primary population (**FIGURE-6A**). The first notable observation is the raw count variability between eTILs exposed to pre-malignant and malignant TMEs, where pre-malignant (Veh-PM/EZH2-PM) have approximately a 20-fold increase compared to eTILs from malignant samples (**FIGURE-1C**). This aligns with the known immune-suppressive environment caused by LSCC. We see the most *Cd8*+ eTILs in EZH2i-M (**FIGURE-6B**) - likely because there is less need for cytotoxic effect in premalignancy. In contrast, *Cd4*+ eTILs are predominantly seen in premalignancy but drop the lowest in EZH2i-M. Further, the ratio of *Cd8*+ to *Cd4*+ is greatest in EZH2i-M and indicates a strong shift to more cytotoxic T cell populations. Importantly, proportions in **FIGURE-6B** do not include *Cd3*+/ *Cd8*-/*Cd4*- populations such as γδ or NK-T. As a complementary approach, we perform trajectory analysis to analyze differentiation and pseudotime (**SUPPLEMENTARY FIGURE-4).**

CellChat revealed changes in eTILs from EZH2i-M that are indicative of an enhanced immune response, while also exhibiting modulatory effects (**FIGURE-6C**). First, heightened antigen responsiveness and cytotoxic capacity due to immune synapse formation are seen with increased (or activated) incoming signals from LCK, MHC-I, FASLG, CEACAM, and CD6. Conversely, reduction (or elimination) of signals from LAMININ, COLLAGEN, FN1,

SELPLG, and ICAM suggests extracellular matrix remodeling and a decrease in tissue retention. That is, eTILs may have more motility within the TME. Further, loss of NOTCH and NKG2D paired with decreased GALECTIN could indicate less terminal differentiation and exhaustion[29]. Hormone shifts are also observed through turned-on DHT and Testosterone, but this is likely due to sex differences in the mice. Intriguingly, we see the potential emergence of compensatory mechanisms because there are clearly decreased immune suppression pathways like TGFb, Prostaglandin, CD52, and CypA, while simultaneously upregulating PD-L1 and CD200. This additionally supports the many ongoing trials combining EZH2i with ICI therapy. Lastly, outgoing signals such as FASLG, CSF, CD6, THY1, and SPP1 indicate a shift to activated and effector-like states, with cross-talk to myeloid compartments.

Similar to[15], we utilized modularity scores in Seurat, directly comparing treatment to vehicle (without multiple comparisons), to determine the stemness and exhaustion of eTILs using *Pdcd1+/Tcf7+/Havcr2-* (i.e. PD1+/TCF1+/Tim3-) and *Pdcd1+/Tcf7-/Havcr2+*, respectively (**FIGURE-6D**). EZH2i increases stemness in both treatment groups, though EZH2i-M did not reach statistical significance (ns, *p=0.08*). When using the *Cd39-/Cd69-* definition of stem-like[30], EZH2i again increases stemness in both treatment groups and EZH2i-M reaches significance (*p=0.04*). Interestingly, environmentally premalignant eTILs experienced an insignificant decrease in exhaustion (*p=0.057)* whereas malignant eTILs were insignificantly more exhausted *(p=0.055)*. Furthermore, we used murine memory markers according to Cell Signaling Technology's *Mouse Immune Cell Marker Guide*[31] to examine memory states (**SUPPLEMENTARY FIGURE-5**). EZH2-PM had significantly more Naïve eTILs than Veh-PM, but EZH2i-M had less (ns) than Veh-M. EZH2-PM was significantly more Activated than Veh-PM, but EZH2i-M had less (ns) than Veh-M. Conversely, EZH2-M was more Cytotoxic (ns) compared to Veh-M, while EZH2-PM was less than Veh-PM (ns). Both treatment groups had more Central Memory eTILs compared to vehicle, though not significantly. EZH2i-M had significantly more Effector Memory compared to Veh-M, but EZH2-PM had significantly less than Veh-PM. The same trend is also seen within the Effector populations.

It is likely that a major contributor to differences in EZH2-PM and EZH2i-M eTIL response is their exposure to pre-malignant and malignant TMEs, respectively. An additional factor is that PM samples were treated for two weeks, whereas M sample samples were treated for four weeks. These data indicate that while EZH2 inhibition is beneficial transiently, pro-longed exposure paired with TME suppression may eventually shift eTILs into terminal differentiation or exhaustion. Determining dosage and timing for optimal TIL response remains an ongoing question under investigation.

DISCUSSION

In this study, we used single-cell resolution to investigate how EZH2 inhibition alters the TME of NSCLC to become more immunogenic. We demonstrated that cell-cell signaling, though weaker overall, was shifted to favor immune populations. In particular, pathways such as MHC-I, FASLG, LCK, and CEACAM were more enriched and active in treatment groups. We also showed downregulation of fibrosis markers in COLLAGEN and FN1. We next inferred TF activities that revealed unique behaviors between groups. In general, transcriptional

programs remained intact, but the factors that make up these programs change activity. For example, we showed shifts in B cell and myeloid differentiation factors and increases in IFN response and apoptosis. Even though we inhibited EZH2 methyltransferase activity, we demonstrated that EZH2 was still very active. This is important because EZH2 has been shown to be essential for T cell development, where knockout leads to terminal differentiation of T cells. Concerning endogenous TIL populations, there were increases in CD8+ and decreases in both CD4+ and Tregs. Pathway alterations revealed incoming and outgoing signals conducive to improved immune response, and eTILs were more stem-like.

Notably, the EZH2 inhibitor used in this study (GSK126) differs from the next generation of inhibitors moving forward in clinical trials (NCT05879484, NCT04102150, 24-LUN-140-DS-PMC). GSK126 failed in clinical trials due to its inability to inhibit tumor growth, a limitation that may partly stem from differences in drug design and delivery compared to new inhibitors. Although GSK126 demonstrates high bioavailability when delivered via intraperitoneal injection in preclinical models, this route is invasive and unsuitable for routine clinical use. Attempts to reformulate the compound for oral administration led to a substantial decrease in bioavailability, whereas Valmetostat (DS-3201) was specifically designed for oral delivery. They also differ in their mechanism of inhibition of EZH2. GSK126 and Valmetostat compete for S-adenosylmethionine (SAM) binding pocket that donates the methyl group allowing EZH2 to carry out its function, but Valemetostat is a dual inhibitor of EZH2/EZH1. Elucidating further mechanisms of Valmetostat could help to explain the variance in effectiveness between the first generation of EZH2 inhibitors and those currently in clinical trials.

While this study has produced new systems-level insights into mechanisms of EZH2 influence on TMEs, there are still some limiting factors that require highlighting. Different resources have different databases and, thus, will produce variable results across methods. First, underrepresentation of certain cell populations impacts the resolution of downstream analysis but still allows for biological insight. CellChat is constrained by its reliance on predefined ligand-receptor databases, which may not capture tissue-specific or context-dependent interactions. Inferred interactions also do not consider heterogeneity within cell groups (e.g. T cell sub-types), nor does CellChat account for potential post-translational modifications. SCENIC is inherently stochastic (GRN inference with regression trees) and relies on pre-computed TF binding motif databases. This results in slight variability in identified regulons, targets, and weights between runs. It also cannot infer actions caused by post-translational activity. Lastly, the pipeline is highly technical, complex, and not particularly user-friendly. Seurat's *AddModuleScore* function for calculating modularity scores is sensitive to gene set composition and size, with larger gene sets prone to inflated scores due to increased probability of capturing non-specific expression patterns. Multiple complementary approaches were employed to help mitigate these limitations.

Future studies will focus on *in vitro* and *in vivo* impact of EZH2 inhibition on TIL production and efficacy. Other works have shown improvement for CAR-T and TCR cellular therapies, but little is known about appropriate dosage and timing with regard to the various phases of TIL production and infusion. Addressing these questions will be critical for development of effective T cell–based immunotherapy strategies for lung cancer patients.

METHODS

Animal work

In vivo murine studies were performed previously[17]. In summary, a mouse model of lung squamous cell carcinoma was generated by deleting both *Lkb1* and *Pten* floxed alleles through adeno-Cre inhalation. After approximately 40 weeks, a baseline MRI scan was performed and mice were assigned to treatment groups. The relevant ones for this study are vehicle (Captisol pH4.6) or GSK126 (300mg/kg) administered as intraperitoneal injections twice per week. Pre-malignant mice received treatment for two weeks while mice with lung tumors received treatment for four weeks. It is also important to note sex differences: Veh-PM (F), EZH2i-PM (F), Veh-M (F), and EZH2i-M (M). All work was approved by the Institutional Animal Care and Use Committee (IACUC) at the University of Kentucky.

Prior single-cell sequencing

To summarize prior work[17], macro-dissected lung tumors from malignant mice, or whole lung tissue from premalignant mice were collected, rapidly mechanically dissociated and run over Miltenyi LS columns to obtain single cell suspension. Single-cell capture was performed with a 10x Genomics Chromium controller and the 10x Genomics Signel cell 3' v3 Kit was used for reverse transcription. Libraries were then prepared and sequenced, and raw sequencing data were aligned to the mm10 mouse genome (v93) using the Cell Ranger v3.1 pipeline (10x Genomics). Downstream analysis was conducted using the Seurat (v3) R package[32]. The workflow consisted of: (1) Quality control and preprocessing – removing genes detected in fewer than three cells, excluding low-quality cells with fewer than 100 detected genes, or those with over 7% mitochondrial transcript content. The filtered expression data were then log-normalized. (2) dataset integration and feature selection – log-normalized matrices from individual samples were merged, and highly variable genes were identified using the variance-stabilizing transformation (VST) method. The top 1,500 variable genes were used for integration. (3) Principal component analysis (PCA) was performed to reduce dimensionality, and cell clusters were identified using a shared nearest neighbor (SNN) graph-based clustering algorithm. (4) Cell identities were assigned by evaluating marker genes uniquely expressed in each cluster.

Differential expression analysis was performed using Seurat's *FindMarkers* function with the Mann-Whitney U test to compare T cell gene expression between EZH2i-M vs Veh-M, EZH2i-PM vs Veh-PM, and EZH2i-M vs EZH2i-PM (**SUPPLEMENTARY**). Genes were considered differentially expressed if they had a log2FC>0.25, were expressed in at least 10% of cells in either group, and significance was determined by adjusted p-value < 0.05.

Functional interpretation of genes, transcription factors (TFs), and pathways was primarily based on publicly available annotations. Unless otherwise stated, biological functions, pathway associations, and regulatory roles were retrieved from GeneCards (www.genecards.org) and NCBI Gene (www.ncbi.nlm.nih.gov/gene). These resources were used for general descriptive purposes and to provide standardized gene function summaries across datasets.

CellChat

To infer and analyze intercellular communication networks, we used CellChat (v2.1.2), a computational tool that leverages scRNAseq data to model ligand-receptor signaling interactions between cell types using a curated database (KEGG and primary literature) [18]. First, scRNAseq data was pre-processed as described above. The resulting expression matrices (split according to resistance group) from the Seurat object were used to create CellChat objects for each treatment arm according to the murine database. CellChat objects were then pre-processed to identify interactions and communication probabilities, including cell-cell and pathway-specific. Note that *interaction* refers to a specific ligand-receptor pair that mediates potential signaling between a sender cell type (expressing the ligand) and a receiver cell type (expressing the receptor). Each interaction is directional and context-dependent. Whereas communication *strength* is a quantitative measure reflecting the total signaling probability between two cell types, often summed over all interactions in a given signaling pathway. It integrates the expression levels of all relevant ligand-receptor pairs and provides a global metric of pathway activity using the law of mass action. All code were written in accordance with the author's vignettes in Rstudio (v4.4.3) (https://github.com/sqjin/CellChat). Significant signaling pathways were identified based on permutation tests and statistical filtering (e.g., p-value < 0.05 unless otherwise stated).

SCENIC

Transcriptional regulatory networks and assessment of transcription factor (TF) activity at the single-cell level was inferred using the Single-Cell rEgulatory Network Inference and Clustering (SCENIC) pipeline to the same top 1500 variable features to make the UMAP in (**FIGURE-1B**). Compared to alternative methods, SCENIC is advantageous because it combines expression analysis with motif enrichment to infer direct (versus correlative) TF-target relationships. In particular, we used the pySCENIC implementation(v0.12.1 - https://github.com/aertslab/pySCENIC) that is performed in three main steps using Spyder (v5.5.1, Python 3.12.7).

First, pySCENIC infers gene co-expression modules using GRNBoost2, a regression-based algorithm that identifies potential regulatory relationships between transcription factors and their target genes based on expression patterns across the dataset. This step generates a list of candidate TF-target interactions without assuming direct binding. Second, these preliminary regulons are refined (i.e. pruned) using cisTarget, which integrates cis-regulatory motif enrichment and genomic annotation data. Only targets with enriched motifs for the corresponding TF are retained, resulting in a high-confidence set of transcription factor–centered modules (also called regulons). Lastly, cells are differentiated and clustered according to regulon activity using AUCell. AUCell calculates the area under the cumulative recovery curve (AUC) for each regulon's gene set in a cell's ranked gene expression profile. This provides a quantitative estimate of regulon activity on a per-cell basis, enabling the identification of cell-type–specific transcriptional programs and dynamic regulatory changes across different cell states.

As with CellChat, treatment groups were analyzed separately and then compared, but with data converted from Seurat objects to loom format for compatibility with pySCENIC. The analysis utilized mouse-specific regulatory databases including ranking databases for cis-regulatory motif analysis (mm9-500bp-upstream, mm9-tss-centered-5kb, and mm9-tss-centered-10kb with 10-species conservation) and a comprehensive transcription factor list (allTFs_mm.txt) containing mouse TF annotations. The three main steps of the pipeline were implemented as described above and Regulon Specificity Scores (RSS) were calculated to identify cell type-specific transcription factors. We also calculated regulon similarities based on target gene overlap using Jaccard similarity metrics.

Complementary methods

Several tools have been developed to infer cell-cell communication from scRNAseq data. However, these often rely on single ligand-receptor pairs, overlooking that many receptors form multi-subunit complexes. Methods such as CellPhoneDB[33] improve this by accounting for receptor subunit expression but still omit key cofactors such as soluble modulators and co-receptors. Additionally, many existing tools lack curated pathway classifications, comprehensive network visualization, support for complex systems analysis, and the ability to capture communication across dynamic cell states. We employed the LIANA[19] (LIgand-receptor ANalysis frAmework) that provides a unified interface for inferring cell-cell communication from single-cell RNA sequencing data by integrating multiple ligand-receptor inference methods and databases. The framework decouples computational methods from their corresponding resources, enabling any combination of 7 different scoring algorithms with 16 distinct ligand-receptor databases, and generates consensus predictions across methods to reduce individual method bias.

BITFAM[21] (Bayesian Inference Transcription Factor Activity Model) is a Bayesian hierarchical framework that infers TF activities in individual cells by integrating scRNAseq data with prior knowledge from ChIP-seq transcription factor binding experiments. The method decomposes log-normalized expression data into matrices representing transcription factor activities and target gene weights using variational inference, where ChIP-seq data provides regulatory prior knowledge through binary matrices indicating predicted target genes for each transcription factor. BITFAM operates on the biological principle that differences in single-cell gene expression profiles reflect distinct underlying transcription factor activity states, enabling identification of regulatory mechanisms and cell clustering based on inferred transcription factor activities rather than gene expression alone.

Lastly, we used CollecTRI[22] (Collection of Transcriptional Regulatory Interactions) which is a comprehensive meta-resource containing signed transcription factor-target gene interactions compiled from 12 different curated databases, providing regulatory relationships for 1,186 transcription factors with mode-of-regulation annotations (activation or inhibition). The resource integrates information from multiple knowledge bases using a systematic workflow to assign regulatory signs to transcription factor-gene interactions, resulting in enhanced coverage and performance in identifying perturbed transcription factors compared to individual databases.

Module scores

Module scores were calculated using the *AddModuleScore()* function in the Seurat R package (v 5.3.0). This method quantifies the relative expression of a predefined gene set within individual cells, facilitating the assessment of pathway activity at the single-cell level. First, we defined our gene set of interest according to phenotypic markers (e.g. *Pdcd1+/Tcf7+/Havcr2-*). To account for both positive and negative markers, combined scores were computed by creating a separate module for negative markers and then subtracting this module score from the positive marker module score. For each cell, the average expression levels of these genes were computed to obtain a module gene expression score. Considering technical variability, including differences in sequencing depth and baseline expression, Seurat generates a control gene set. This background set consists of randomly selected genes matched to the module genes by overall expression level. The final module score for each cell was then calculated as the difference between the mean expression of the module genes and the mean expression of the matched control genes.

GRN inference and analysis

Regulatory networks were inferred from scRNAseq data using GRNboost2[34], which employs gradient-boosting machines to model expression of genes based on candidate TFs. For every target gene, it constructs a regression model using shallow decision trees, where each tree is trained on a random subset of the data (90%) and evaluated on the remaining 10%. New trees are added iteratively until the average improvement of prediction falls below zero. Importance scores of TFs in predicting target gene expression are aggregated across all models to produce a final ranked regulatory network.

Once a GRN was created, analysis was performed using NetworkX (v3.4.2) and Pyvis (v0.3.2) in Python. The top 500 TF-target interactions ranked by importance score were used to construct directed and weighted (but not signed) networks. Nodes were classified as transcription factors (TFs), target genes, or dual-role genes (acting as both TF and target), with network topology analyzed through standard graph theory metrics including degree distribution, connectivity patterns, and component structure. Weakly and strongly connected components were identified to assess network fragmentation, while centrality measures (betweenness and closeness centrality) were calculated to identify key regulatory hubs and bridge nodes. Edge weight statistics characterized the distribution of regulatory interaction strengths, and network motifs including self-loops (auto-regulation) and mutual regulation pairs were quantified. Master regulators were identified as nodes with the highest out-degree (number of target genes regulated), while the most regulated genes were determined by in-degree (number of incoming regulatory connections). Interactive network visualizations were generated with Pyvis, incorporating physics-based layout algorithms and node/edge styling based on functional classifications and interaction strengths.

Phenotype control theory using feedback vertex set (FVS)[27] was also used. As previously mentioned, the inferred GRN has no inherent update functions, and we must rely on topological structures to find targets. In FVS control, by pinning a subset of nodes that intersect every cycle in the network, we disrupt all feedbacks, making

the resulting network admit a single steady state. In other words, a FVS of a graph is a minimal set of nodes whose removal leaves the graph without cycles[24].

Trajectories and pseudotime

Trajectory analysis was performed using Monocle3(v1.3.7) to infer differentiation velocities within T cell populations. T cell subsets were extracted from the integrated Seurat object, merged according to vehicle or treatment, and converted to a *cell_data_set* object. Dimensionality reduction was performed using principal component analysis followed by UMAP embedding. Cells were clustered using the Louvain algorithm and assigned to partitions. Trajectory graphs were learned using the SimplePPT algorithm, and cells were ordered along pseudotime after manual selection of root nodes corresponding to naive/early T cell states based on Tcf7. Differential gene expression along the trajectory was assessed using Moran's I test to identify genes with significant expression changes as a function of pseudotime. All analyses were performed separately for each treatment group to enable comparative trajectory analysis. This can be seen in **SUPPLEMENTARY FIGURE-5**

Statistics and reproducibility

Statistical tests were performed in Python, R, or Excel. Each of the primary methods employed incorporates its own inherent statistical techniques within its framework, including multiple testing adjustments. Please refer to the corresponding publications for more details (all directly linked in GitHub). For pairwise comparison of modules and GRN importance between treatment groups, we used the Mann-Whitney U test. Resulting p-values for modules were adjusted for multiple testing using Benjamini-Hochberg. Normality was evaluated with the Shapiro-Wilk test, and effect size was determined by Cliff's δ.

DATA AVAILABILITY

All data presented in this article are available from the corresponding author upon reasonable request. The sequencing data are available at NCBI Gene Expression Omnibus under the super-series GSE233665, and full method-specific results are available at (https://github.com/drplaugher/EZH2_scRNAseq_signaling).

CODE AVAILABILITY

All code used in this article are available from the corresponding author upon reasonable request. The scripts build upon publicly available vignettes provided by the respective original authors in their published repositories. Modifications and additions specific to this work are available on the GitHub repository, along with instructions for reproducing the results. Proper attribution to the original sources is provided within the repository.

ACKNOWLEDGEMENTS

The authors have no acknowledgments to declare.

Funding

This work was supported in part by NCI K99CA303792 (DRP), NCI T32-CA165990 (DRP, CMG), National Center for Advancing Translational Sciences - NIH UL1TR001998 (DRP, CFB), R01-CA237643 (CFB), and R01-HL170193 (CFB). This research was also supported by the Biostatistics & Bioinformatics Shared Resource Facility, Cancer Research Informatics, Oncogenomics Shared Resource Facility, Biospecimen Procurement & Translational Pathology Shared Resource Facility and Flow Cytometry & Immune Monitoring Shared Resource Facility of the University of Kentucky Markey Cancer Center (P30-CA177558). The content is solely the responsibility of the authors and does not necessarily represent the official views of the NIH.

Author Contributions

Conceptualization: DRP, CFB; Data Curation: DRP; Data acquisition and processing: DRP, JL, CFB; Formal analysis: DRP, AC, CMG, CFB; Bioinformatics and biostatistics: DRP, JL; Writing – original draft: DRP, CFB, AC; Writing – review and editing: DRP, CFB, AC, CMG, DPE

Ethics Declarations

The authors declare no competing interests.

Supplementary Information

See the **Supplementary File** and GitHub repository.

FIGURES AND LEGENDS

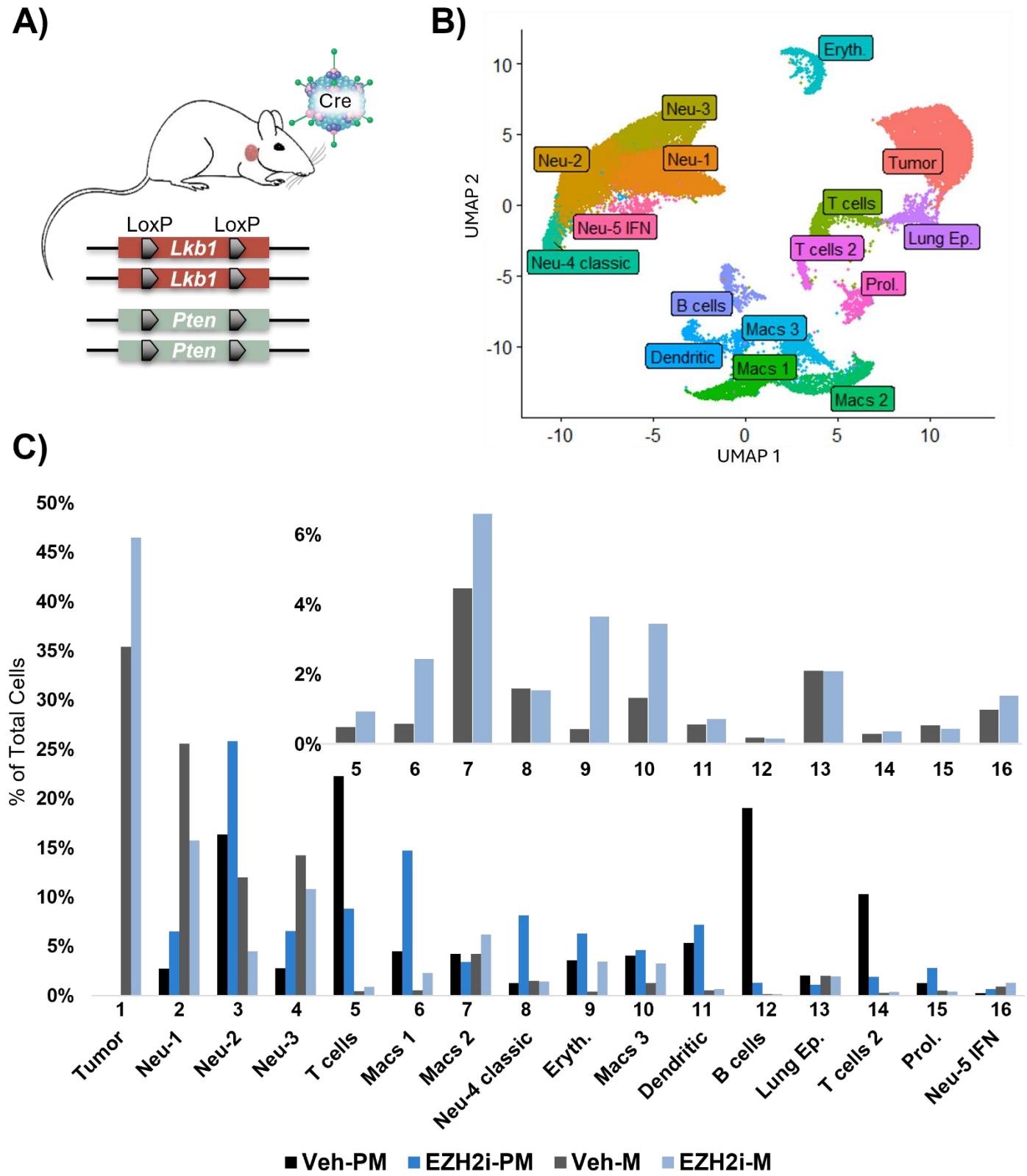

Fig. 1: Single-cell profiling of TME. **A)** Schematic: Generation of murine autochthonous squamous lung cancer induced in *Lkb1/Pten* mice by adenoCre administration. **B)** Annotated UMAP showing 16 populations within lung tumors after treatment with Veh-PM, EZH2i-PM, Veh-M, or EZH2i-M. **C)** Percentage of annotated cells per treatment group graphed for all populations, zoomed subgraph only shows Veh-M and EZH2i-M.

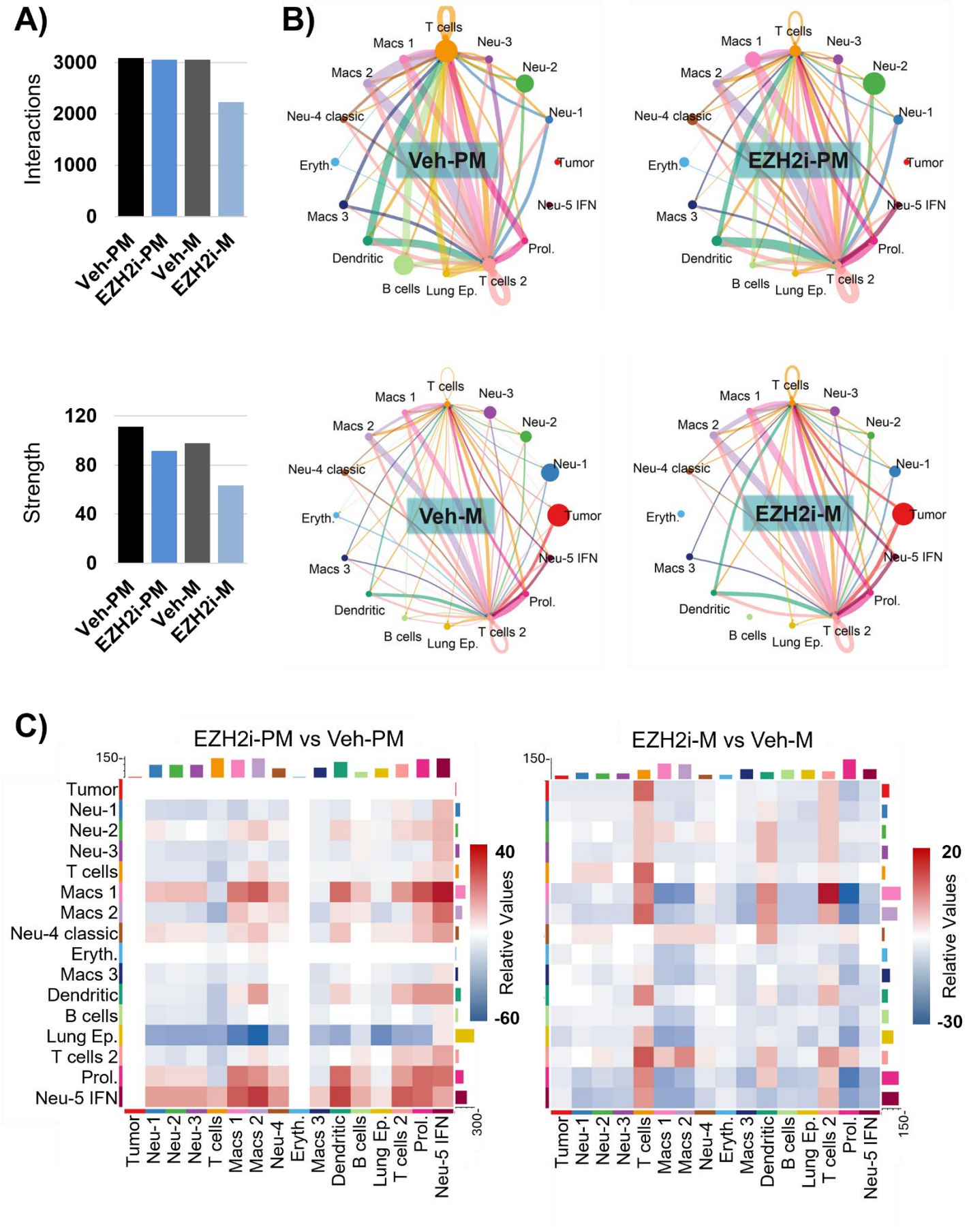
A)
Interactions
3000
2000
1000
0
Veh-PM
EZH2i-PM
Veh-M
EZH2i-M
Strength
120
80
40
0
B)
Veh-PM
EZH2i-PM
Veh-M
EZH2i-M
T cells
Macs 1
Neu-3
Neu-2
Macs 2
Neu-1
Neu-4 classic
Eryth.
Tumor
Neu-5 IFN
Macs 3
Prol.
Dendritic
B cells
Lung Ep.
T cells 2
C)
EZH2i-PM vs Veh-PM
EZH2i-M vs Veh-M
Relative Values
40
-60
20
-30
150
300
Tumor
Neu-1
Neu-2
Neu-3
T cells
Macs 1
Macs 2
Neu-4
Eryth.
Macs 3
Dendritic
B cells
Lung Ep.
T cells 2
Prol.
Neu-5 IFN

Fig. 2: Cell-cell communication patterns. **A)** Total number of interactions and interaction strengths of the inferred cell-cell communication networks between conditions. **B)** Aggregated cell-cell communications focusing on TME signals to and from T cells. Edge colors are consistent with senders, edge weights are proportional to interaction strength, and circle sizes are proportional to the number of cells in each cell group. **C)** Differential interaction heatmaps, where red (or blue) represents increased (or decreased) signaling in treatment compared to vehicle. The top-colored bar plot represents the column sum of values displayed in the heatmap (incoming signaling) and right colored bar plots represent the sum of row of values (outgoing signaling).

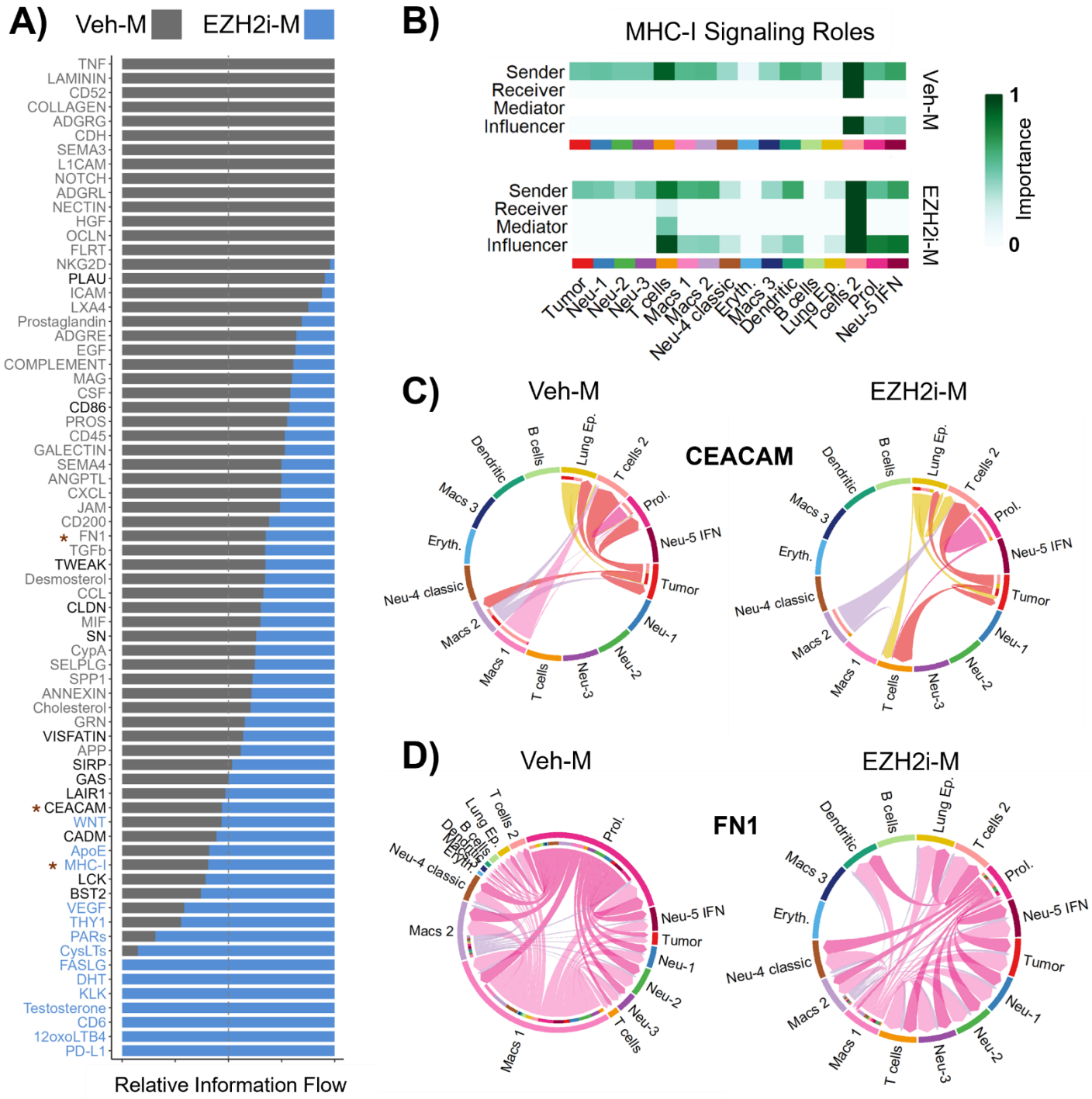

Fig. 3: Dynamic pathway communications among malignant samples. **A)** Conserved and context-specific relative information flow alterations for highly significant (p<0.01) pathways. Pathways colored gray are enriched in Veh-M, blue is enriched in EZH2i-M, and text colored black indicates an enriched pathway in both groups. Red stars are markers for pathways highlighted in remaining sub-figures. B) Major network signaling roles of MHC-I between TME components. **C&D)** Chord diagrams showing signaling for CEACAM and FN1 (respectively) between cell groups, where inner thinner bar colors represent the targets that receive signal from the corresponding outer bar. Inner bar size is proportional to the signal strength received by the targets.

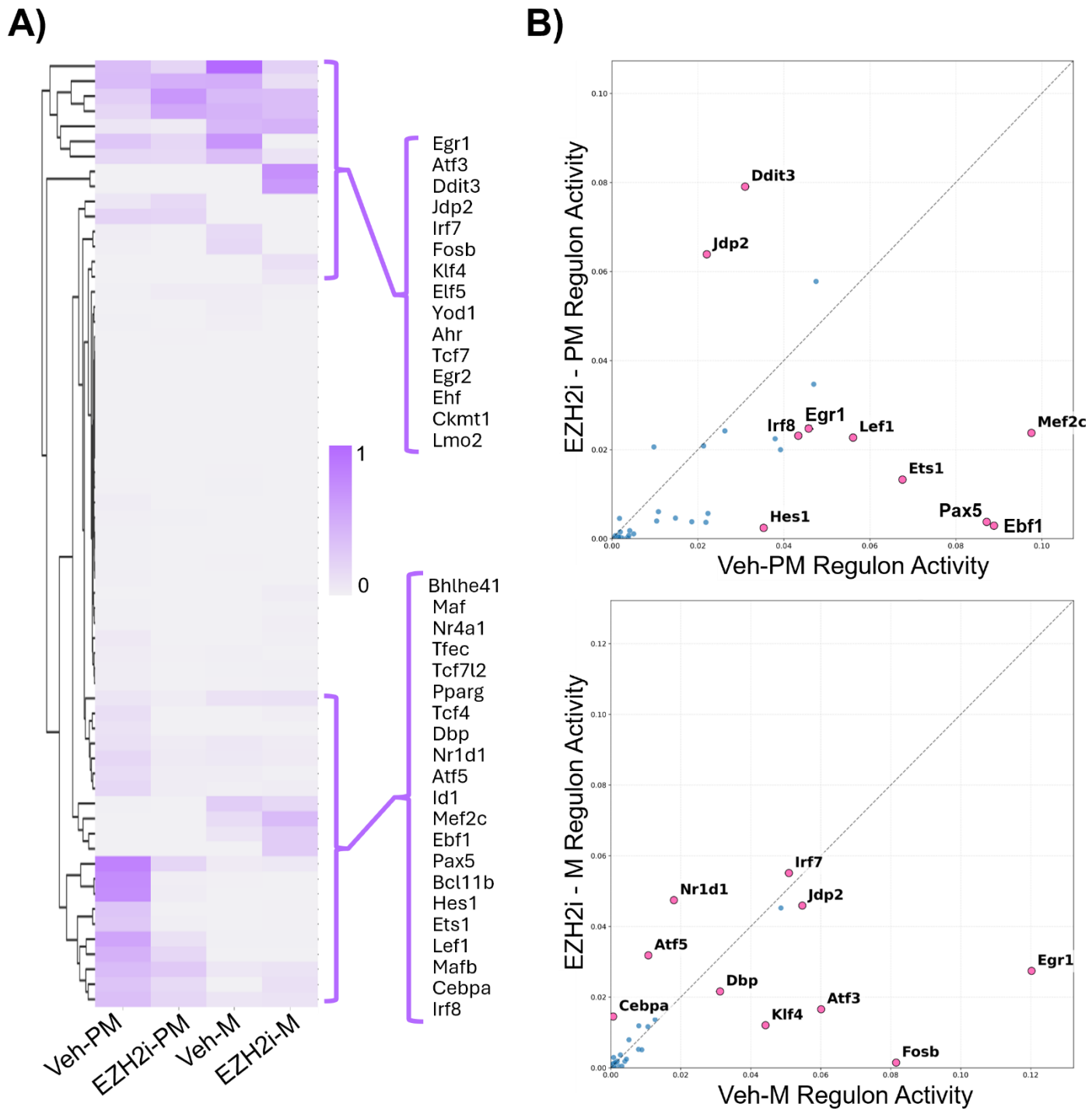

Fig. 4: Overall inferred transcriptional activity. **A)** Heatmap of normalized-clustered activity signatures of all conditions. **B)** Scatter plots comparing shared TF activity between treatment (y) and vehicle (x) among pre-malignant and malignant conditions. TFs highlighted are the top 10 most differentially active (absolute difference).

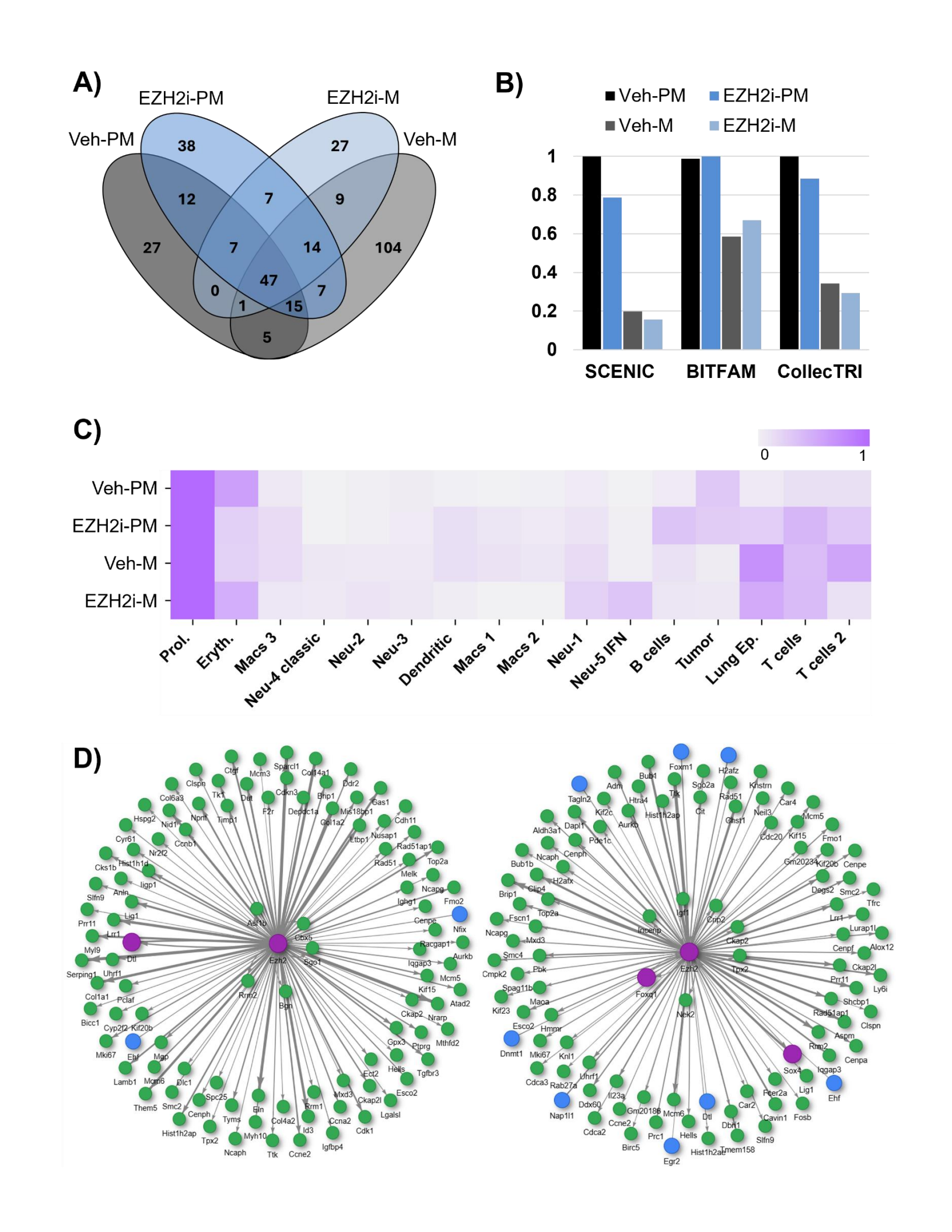
A)
EZH2i-PM
EZH2i-M
Veh-PM
Veh-M
38
27
12
7
9
27
7
14
104
47
0
7
1
15
5
B)
Veh-PM
EZH2i-PM
Veh-M
EZH2i-M
1
0.8
0.6
0.4
0.2
0
SCENIC
BITFAM
CollecTRI
C)
0
1
Veh-PM
EZH2i-PM
Veh-M
EZH2i-M
Prol.
Eryth.
Macs 3
Neu-4 classic
Neu-2
Neu-3
Dendritic
Macs 1
Macs 2
Neu-1
Neu-5 IFN
B cells
Tumor
Lung Ep.
T cells
T cells 2
D)
Ezh2
Asf1b
Cbx5
Sgo1
Rrm2
Bgn
Dtl
Lig1
Lrr1
Ehf
Foxq1
Sox4
Igf1
Cnp2
Ckap2
Tpx2
Nek2
Incenp
Top2a
Fscn1
Mxd3
Smc4
Pbk
Spag11b
Maoa
Esco2
Hmmr
Knl1
Uhrf1
Rab27a
Ddx60
Il23a
Gm20186
Mcm6
Ccne2
Cdca2
Birc5
Prc1
Hells
Hist1h2ae
Tmem158
Egr2
Dbn1
Slfn9
Cavin1
Fosb
Lig1
Fcer2a
Car2
Iqgap3
Cenpa
Rrm2
Aspm
Clspn
Rad51ap1
Shcbp1
Ly6i
Prr11
Ckap2l
Alox12
Cenpf
Lurap1l
Tfrc
Smc2
Degs2
Cenpe
Kif20b
Gm20234
Kif15
Fmo1
Mcm5
Car4
Knstrn
Rad51
Sgo2a
Ttk
Cit
Cnst1
Neil3
Cdc20
Hist1h2ap
Htra4
Aurkb
Kif2c
Pde1c
Cenph
Ncaph
Bub1b
H2afx
Clip4
Brip1
Dapl1
Aldh3a1
Tagln2
Adm
Bub1
Foxm1
H2afz
Ncapg
Mki67
Cdca3
Knl1
Esco2
Dnmt1
Cmpk2
Kif23
Ehf
Nap1l1
Dtl
Car2
Dbn1
Cdk1
Lgalsl
Esco2
Ckap2l
Mxd3
Rrm1
Ccna2
Id3
Igfbp4
Ccne2
Ttk
Ncaph
Myh10
Tpx2
Tyms
Col4a2
Gln
Spc25
Smc2
Cenph
Hist1h2ap
Dlc1
Mcm6
Them5
Lamb1
Mgp
Mki67
Cyp2f2
Kif20b
Bicc1
Pclaf
Col1a1
Uhrf1
Serping1
Myl9
Prr11
Cks1b
Hist1h1d
Cyr61
Nr2f2
Hspg2
Nid1
Col6a3
Clspn
Ctgf
Mcm3
Sparcl1
Col14a1
Ddr2
Cdkn3
Bhlp1
Gas1
Cdh11
Nusap1
Rad51ap1
Top2a
Rad51
Melk
Ncapg
Fmo2
Nfix
Aurkb
Atad2
Mthfd2
Tgfbr3
Hells
Gpx3
Ptprg
Nrarp
Ckap2
Kif15
Mcm5
Iqgap3
Racgap1
Cenpe
Ighg1
Ttk
Cit
Htra4
Hist1h2ap
Aurkb
Kif2c
Pde1c
Cenph
Ncaph
Bub1b
H2afx
Clip4
Top2a
Fscn1
Mxd3
Smc4
Pbk
Spag11b
Maoa
Esco2
Hmmr
Knl1
Uhrf1
Rab27a
Ddx60
Il23a
Gm20186
Mcm6
Ccne2
Cdca2
Birc5
Prc1
Hells
Hist1h2ae
Tmem158
Egr2
Dtl
Car2
Dbn1
Cdk1
Lgalsl
Esco2
Ckap2l
Mxd3
Rrm1
Ccna2
Id3
Igfbp4
Ccne2
Ttk
Ncaph
Myh10
Tpx2
Tyms
Col4a2
Gln
Spc25
Smc2
Cenph
Hist1h2ap
Dlc1
Mcm6
Them5
Lamb1
Mgp
Mki67
Cyp2f2
Kif20b
Bicc1
Pclaf
Col1a1
Uhrf1
Serping1
Myl9
Prr11
Cks1b
Hist1h1d
Cyr61
Nr2f2
Hspg2
Nid1
Col6a3
Clspn
Ctgf
Mcm3
Sparcl1
Col14a1
Ddr2
Cdkn3
Bhlp1
Gas1
Cdh11
Nusap1
Rad51ap1
Top2a
Rad51
Melk
Ncapg
Fmo2
Nfix
Aurkb
Atad2
Mthfd2
Tgfbr3
Hells
Gpx3
Ptprg
Nrarp
Ckap2
Kif15
Mcm5
Iqgap3
Racgap1
Cenpe
Ighg1
Ttk
Cit
Htra4
Hist1h2ap
Aurkb
Kif2c
Pde1c
Cenph
Ncaph
Bub1b
H2afx
Clip4
Brip1
Dapl1
Aldh3a1
Tagln2
Adm
Bub1
Foxm1
H2afz
Ncapg
Mki67
Cdca3
Knl1
Esco2
Dnmt1
Cmpk2
Kif23
Ehf
Nap1l1

Fig. 5: Ezh2 inferred transcriptional activity among conditions. **A)** 4-way Venn diagram of total shared targets. **B)** Overall levels of normalized Ezh2 activity using three inference methods. **C)** Clustered heatmap of cell type-specific Ezh2 activity. D) Gene regulatory network of top 100 Ezh2 interactions, where we indicate target genes (green), transcription factors signaling to *Ezh2* (blue), and dual-role actors that crosstalk with *Ezh2* (purple). An interactive version is available on our GitHub repository.

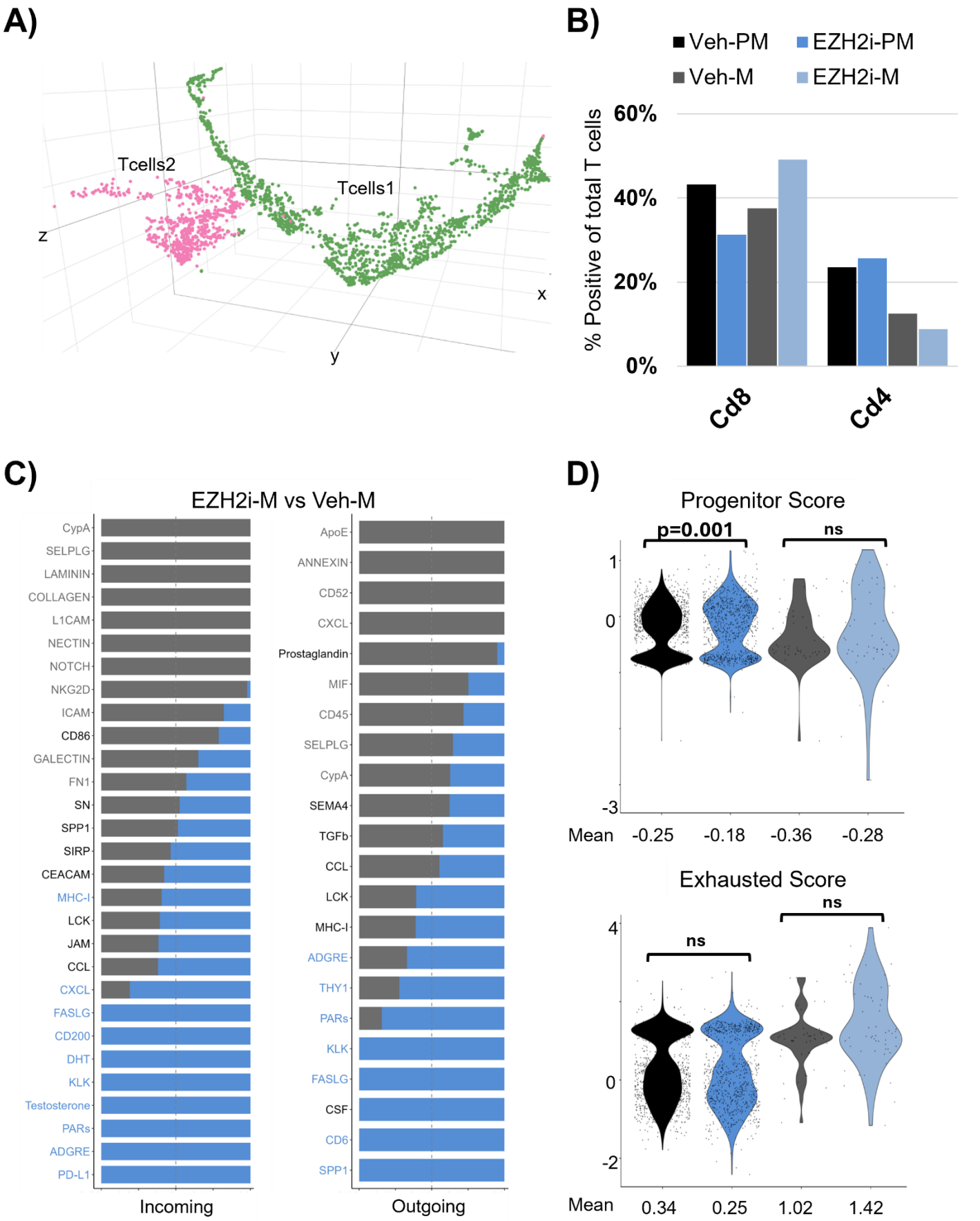
A)
Tcells2
Tcells1
z
x
y
B)
Veh-PM
EZH2i-PM
Veh-M
EZH2i-M
% Positive of total T cells
60%
40%
20%
0%
Cd8
Cd4
C)
EZH2i-M vs Veh-M
CypA
SELPLG
LAMININ
COLLAGEN
L1CAM
NECTIN
NOTCH
NKG2D
ICAM
CD86
GALECTIN
FN1
SN
SPP1
SIRP
CEACAM
MHC-I
LCK
JAM
CCL
CXCL
FASLG
CD200
DHT
KLK
Testosterone
PARs
ADGRE
PD-L1
ApoE
ANNEXIN
CD52
CXCL
Prostaglandin
MIF
CD45
SELPLG
CypA
SEMA4
TGFb
CCL
LCK
MHC-I
ADGRE
THY1
PARs
KLK
FASLG
CSF
CD6
SPP1
Incoming
Outgoing
D)
Progenitor Score
p=0.001
ns
1
0
-3
Mean
-0.25
-0.18
-0.36
-0.28
Exhausted Score
ns
ns
4
0
-2
Mean
0.34
0.25
1.02
1.42

Fig. 6: Endogenous TIL alterations. A) 3-dimensional UMAP of T cell populations. B) Proportions of T cells positive for Cd8 (Cd8α/β) and Cd4 (including Foxp3). **C)** Conserved and context-specific relative information flow alterations for highly significant ($p<0.01$) pathways incoming and outgoing from eTILs. Pathways colored gray are enriched in Veh-M, blue is enriched in EZH2i-M, and text colored black indicates an enriched pathway in both groups. **D)** Violin plots of module scores comparing progenitor (*Pdcd1+/Tcf7+/Havcr2-*) and exhausted (*Pdcd1+/Tcf7-/Havcr2+*) phenotypes.

References

1. Siegel RL, Kratzer TB, Giaquinto AN, Sung H, Jemal A. Cancer statistics, 2025. CA: A Cancer Journal for Clinicians. 2025;75(1):10-45.
2. Rosenberg SA, Restifo NP. Adoptive cell transfer as personalized immunotherapy for human cancer. Science. 2015;348(6230):62-8.
3. Rosenberg SA, Parkhurst MR, Robbins PF. Adoptive cell transfer immunotherapy for patients with solid epithelial cancers. Cancer Cell. 2023;41(4):646-8.
4. Plaugher DR, Childress AR, Gosser CM, Esoe D-P, Naughton KJ, Hao Z, Brainson CF. Therapeutic potential of tumor-infiltrating lymphocytes in non-small cell lung cancer. Cancer Letters. 2024:217281.
5. Henning AN, Roychoudhuri R, Restifo NP. Epigenetic control of CD8+ T cell differentiation. Nature Reviews Immunology. 2018;18(5):340-56.
6. McCabe MT, Ott HM, Ganji G, Korenchuk S, Thompson C, Van Aller GS, et al. EZH2 inhibition as a therapeutic strategy for lymphoma with EZH2-activating mutations. Nature. 2012;492(7427):108-12.
7. Italiano A, Soria J-C, Toulmonde M, Michot J-M, Lucchesi C, Varga A, et al. Tazemetostat, an EZH2 inhibitor, in relapsed or refractory B-cell non-Hodgkin lymphoma and advanced solid tumours: a first-in-human, open-label, phase 1 study. The Lancet Oncology. 2018;19(5):649-59.
8. Hoy SM. Tazemetostat: First Approval. Drugs. 2020;80(5):513-21.
9. Zinzani PL, Izutsu K, Mehta-Shah N, Barta SK, Ishitsuka K, Córdoba R, et al. Valemetostat for patients with relapsed or refractory peripheral T-cell lymphoma (VALENTINE-PTCL01): a multicentre, open-label, single-arm, phase 2 study. The Lancet Oncology. 2024;25(12):1602-13.
10. Gray SM, Amezquita RA, Guan T, Kleinstein SH, Kaech SM. Polycomb Repressive Complex 2-Mediated Chromatin Repression Guides Effector CD8(+) T Cell Terminal Differentiation and Loss of Multipotency. Immunity. 2017;46(4):596-608.
11. He S, Liu Y, Meng L, Sun H, Wang Y, Ji Y, et al. Ezh2 phosphorylation state determines its capacity to maintain CD8(+) T memory precursors for antitumor immunity. Nature communications. 2017;8(1):2125.
12. DuPage M, Chopra G, Quiros J, Rosenthal WL, Morar MM, Holohan D, et al. The Chromatin-Modifying Enzyme Ezh2 Is Critical for the Maintenance of Regulatory T Cell Identity after Activation. Immunity. 2015;42(2):227-38.
13. Wang D, Quiros J, Mahuron K, Pai C-C, Ranzani V, Young A, et al. Targeting EZH2 Reprograms Intratumoral Regulatory T Cells to Enhance Cancer Immunity. Cell Rep. 2018;23(11):3262-74.
14. Goswami S, Apostolou I, Zhang J, Skepner J, Anandhan S, Zhang X, et al. Modulation of EZH2 expression in T cells improves efficacy of anti-CTLA-4 therapy. J Clin Invest. 2018;128(9):3813-8.
15. Hou Y, Zak J, Shi Y, Pratumchai I, Dinner B, Wang W, et al. Transient EZH2 Suppression by Tazemetostat during In Vitro Expansion Maintains T-Cell Stemness and Improves Adoptive T-Cell Therapy. Cancer Immunol Res. 2025;13(1):47-65.

16. Porazzi P, Nason S, Yang Z, Carturan A, Ghilardi G, Guruprasad P, et al. EZH1/EZH2 inhibition enhances adoptive T cell immunotherapy against multiple cancer models. Cancer Cell. 2025;43(3):537-51.e7.

17. DuCote TJ, Song X, Naughton KJ, Chen F, Plaugher DR, Childress AR, et al. EZH2 inhibition promotes tumor immunogenicity in lung squamous cell carcinomas. Cancer Research Communications. 2024.

18. Jin S, Guerrero-Juarez CF, Zhang L, Chang I, Ramos R, Kuan C-H, et al. Inference and analysis of cell-cell communication using CellChat. Nature Communications. 2021;12(1):1088.

19. Dimitrov D, Türei D, Garrido-Rodriguez M, Burmedi PL, Nagai JS, Boys C, et al. Comparison of methods and resources for cell-cell communication inference from single-cell RNA-Seq data. Nature Communications. 2022;13(1):3224.

20. Van de Sande B, Flerin C, Davie K, De Waegeneer M, Hulselmans G, Aibar S, et al. A scalable SCENIC workflow for single-cell gene regulatory network analysis. Nature Protocols. 2020;15(7):2247-76.

21. Gao S, Dai Y, Rehman J. A Bayesian inference transcription factor activity model for the analysis of single-cell transcriptomes. Genome Res. 2021;31(7):1296-311.

22. Müller-Dott S, Tsirvouli E, Vazquez M, Ramirez Flores Ricardo O, Badia-i-Mompel P, Fallegger R, et al. Expanding the coverage of regulons from high-confidence prior knowledge for accurate estimation of transcription factor activities. Nucleic Acids Research. 2023;51(20):10934-49.

23. Yang L, Liu Y, Zhang B, Yu M, Huang F, Zeng J, et al. CEACAM1 Is a Prognostic Biomarker and Correlated with Immune Cell Infiltration in Clear Cell Renal Cell Carcinoma. Dis Markers. 2023;2023:3606362.

24. Plaugher D, Murrugarra D. Phenotype Control techniques for Boolean gene regulatory networks. Bull Math Biol. 2023;85(10):89.

25. Murrugarra D, Veliz-Cuba A, Aguilar B, Laubenbacher R. Identification of control targets in Boolean molecular network models via computational algebra. BMC Syst Biol. 2016;10(1):94.

26. Yang G, Gómez Tejeda Zañudo J, Albert R. Target Control in Logical Models Using the Domain of Influence of Nodes. Front Physiol. 2018;9:454.

27. Zañudo JGT, Yang G, Albert R. Structure-based control of complex networks with nonlinear dynamics. Proc Natl Acad Sci U S A. 2017;114(28):7234-9.

28. Czystowska-Kuzmicz M, Sosnowska A, Nowis D, Ramji K, Szajnik M, Chlebowska-Tuz J, et al. Small extracellular vesicles containing arginase-1 suppress T-cell responses and promote tumor growth in ovarian carcinoma. Nature communications. 2019;10(1):3000.

29. Amsen D, Helbig C, Backer RA. Notch in T Cell Differentiation: All Things Considered. Trends Immunol. 2015;36(12):802-14.

30. Krishna S, Lowery FJ, Copeland AR, Bahadiroglu E, Mukherjee R, Jia L, et al. Stem-like CD8 T cells mediate response of adoptive cell immunotherapy against human cancer. Science. 2020;370(6522):1328-34.

31. Technology CS. Mouse Immune Cell Marker Guide 2021 [updated February 26, 2021. Available from: https://www.cellsignal.com/pathways/immune-cell-markers-mouse.

32. Stuart T, Butler A, Hoffman P, Hafemeister C, Papalexi E, Mauck WM, 3rd, et al. Comprehensive Integration of Single-Cell Data. Cell. 2019;177(7):1888-902 e21.

33. Troulé K, Petryszak R, Cakir B, Cranley J, Harasty A, Prete M, et al. CellPhoneDB v5: inferring cell–cell communication from single-cell multiomics data. Nature Protocols. 2025.

34. Moerman T, Aibar Santos S, Bravo González-Blas C, Simm J, Moreau Y, Aerts J, Aerts S. GRNBoost2 and Arboreto: efficient and scalable inference of gene regulatory networks. Bioinformatics. 2018;35(12):2159-61.

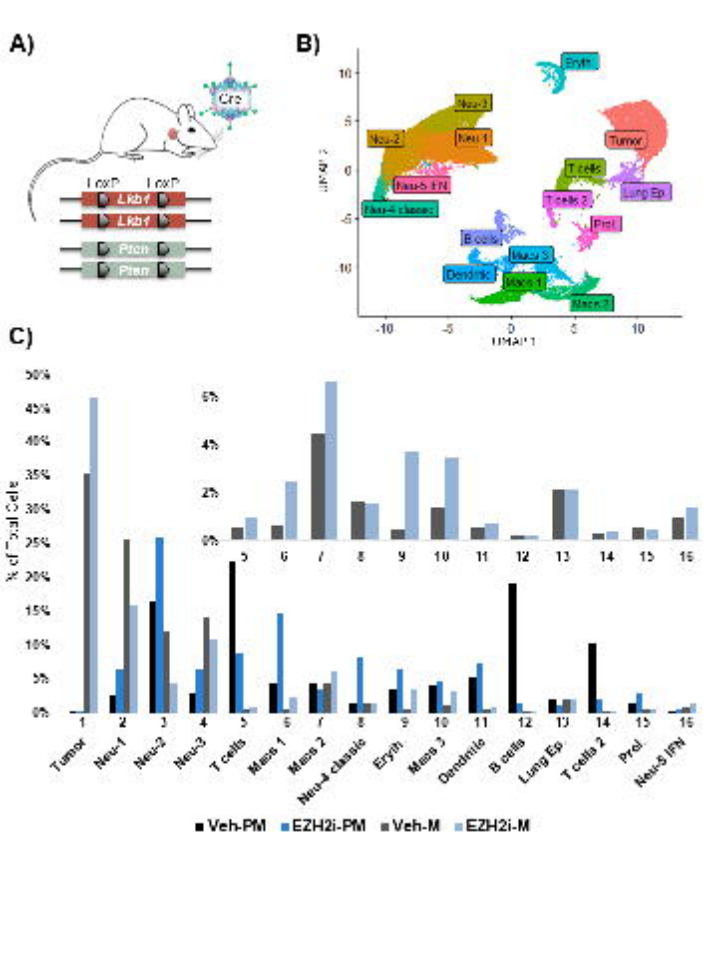
A)
Cre
LoxP
LoxP
Lkb1
Lkb1
Pten
Pten
B)
Eryth
Neu-3
Neu-2
Neu-1
Tumor
T cells
Neu-5 IFN
T cells 2
Lung Ep
Neu-4 classic
Prol
B cells
Macs 3
Dendritic
Macs 1
Macs 2
UMAP 2
UMAP 1
C)
% of Total Cells
Tumor
Neu-1
Neu-2
Neu-3
T cells
Macs 1
Macs 2
Neu-4 classic
Eryth
Macs 3
Dendritic
B cells
Lung Ep
T cells 2
Prol
Neu-5 IFN
Veh-PM
EZH2i-PM
Veh-M
EZH2i-M

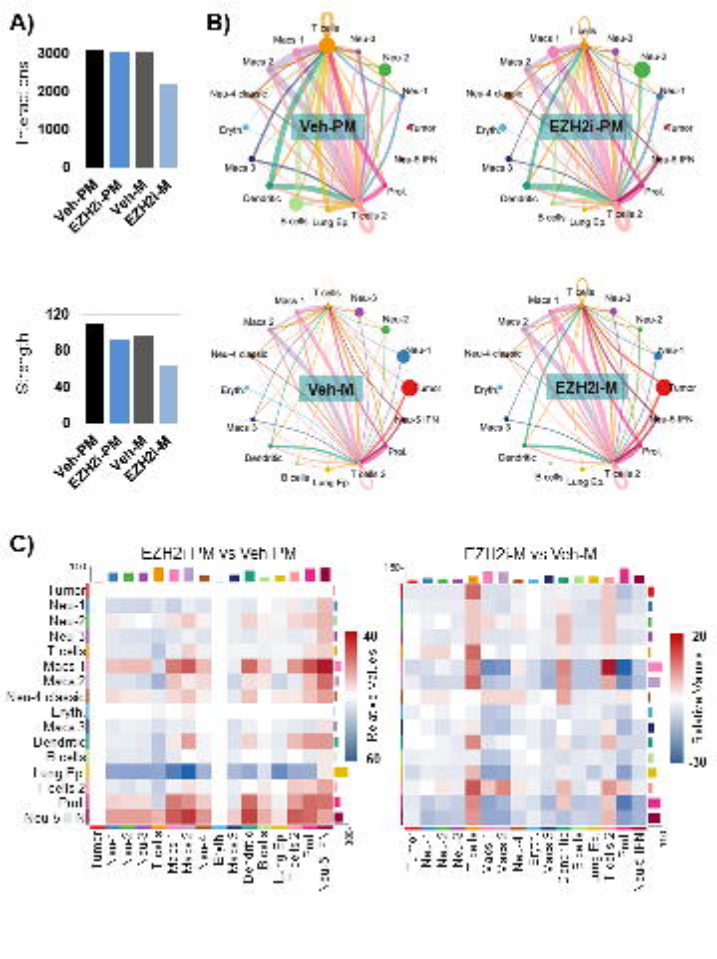
A)
B)
C)
Veh-PM
EZH2i-PM
Veh-M
EZH2i-M
Strength
EZH2i-PM vs Veh-PM
EZH2i-M vs Veh-M
Relative Values

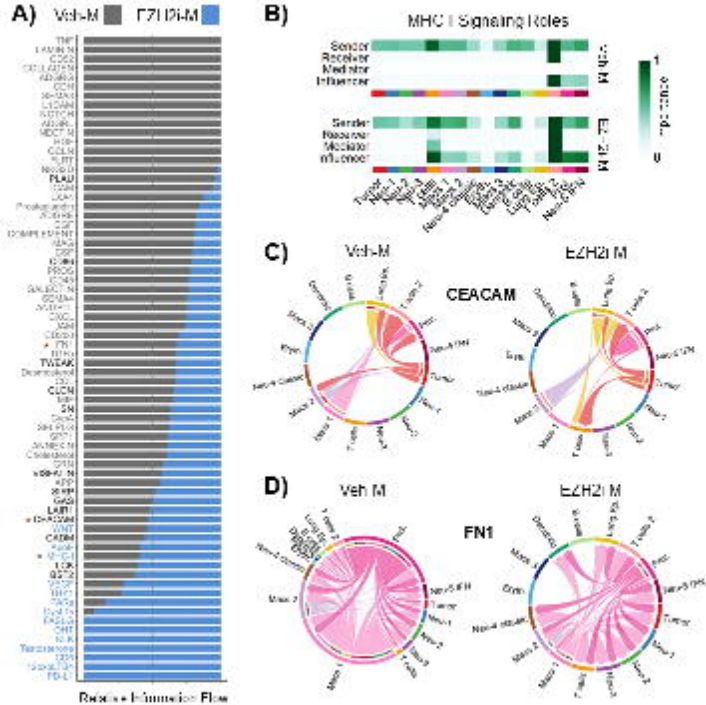
A)
Veh-M
EZH2i-M
Relative Information Flow
B)
MHC I Signaling Roles
Sender
Receiver
Mediator
Influencer
Veh-M
EZH2i-M
C)
Veh-M
EZH2i-M
CEACAM
D)
Veh-M
EZH2i-M
FN1

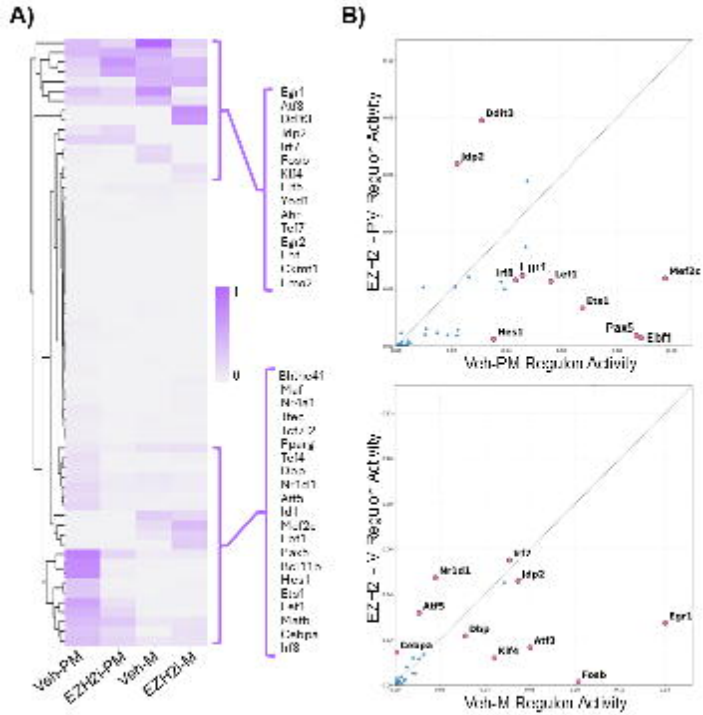
A)
B)
Veh-PM
EZH2i-PM
Veh-M
EZH2i-M
Veh-PM Regulon Activity
Veh-M Regulon Activity

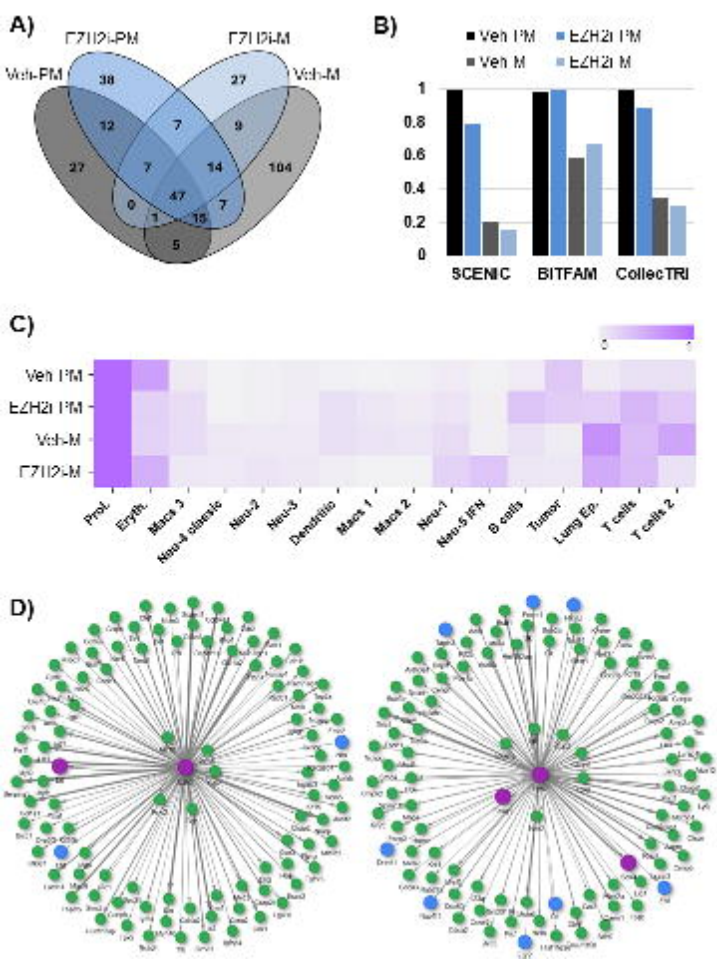
A)
EZH2i-PM
EZH2i-M
Veh-PM
Veh-M
38
27
12
7
9
27
7
14
104
47
0
7
1
15
5
B)
Veh PM
EZH2i PM
Veh M
EZH2i M
1
0.8
0.6
0.4
0.2
0
SCENIC
BITFAM
CollecTRI
C)
Veh PM
EZH2i PM
Veh-M
EZH2i-M
Prol.
Eryth.
Macs 3
Neu-4 classic
Neu-2
Neu-3
Dendritic
Macs 1
Macs 2
Neu-1
Neu-5 IFN
B cells
Tumor
Lung Ep.
T cells
T cells 2
D)

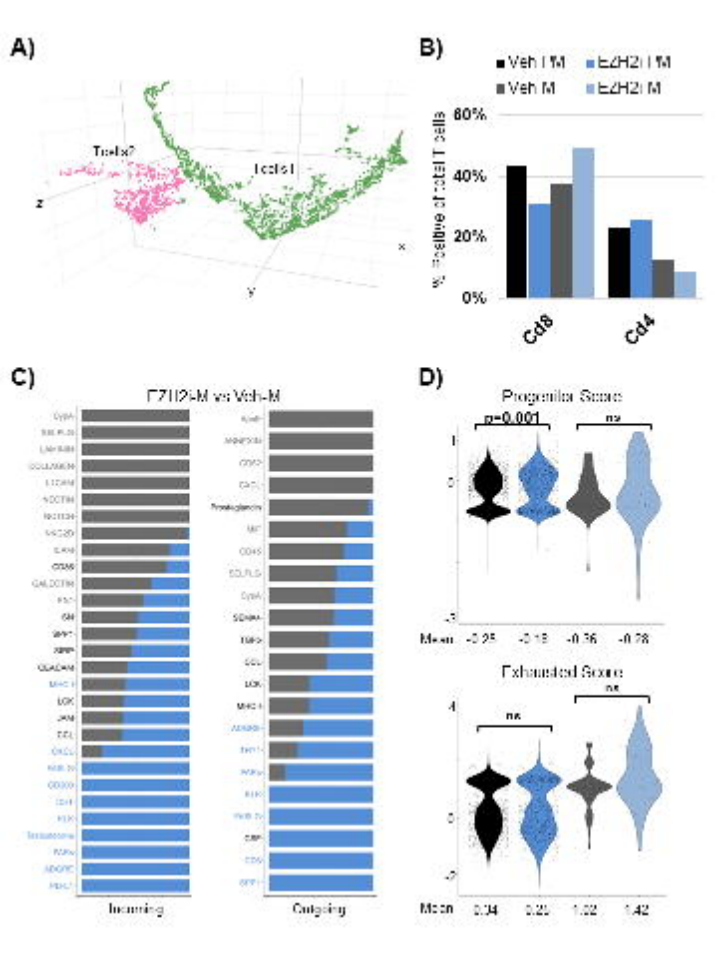
A)
Tcells2
Tcells1
z
x
y
B)
Veh I M
EZH2i I M
Veh M
EZH2i M
80%
40%
20%
0%
% Positive of total T cells
Cd8
Cd4
C)
EZH2i-M vs Veh-M
Incoming
Outgoing
D)
Progenitor Score
p=0.001
ns
Mean
-0.25
-0.18
-0.36
-0.28
Exhausted Score
ns
ns
Mean
0.34
0.21
1.02
1.42